RESEARCH ON OPTIMIZATION OF ANNULAR FIN PHASE CHANGE HEAT STORAGE DEVICE BASED ON ORTHOGONAL TEST

Jiaojin XU**，*Lihua CAO*，*Chenxi BAI*，*Pan LI

School of Energy and Power Engineering, Northeast Electric Power University, Jilin, China;

This study investigates the impact of structural parameters on the heat storage capacity of an annular fin phase change heat storage (PCHS) device. Utilizing a quadratic regression orthogonal experiment combined with numerical simulation, a reliable regression equation was developed to optimize the structural parameters of the heat storage device. The performance of heat storage and release characteristics under optimal structural conditions was further explored by varying operating parameters. The results demonstrate that the radius of the steam pipe, fin thickness, and fin length significantly impact the heat storage capacity, and an optimal set of structural parameters exists that maximizes heat storage. During the heat storage process, increasing the steam mass flow rate and inlet temperature accelerates the melting of phase change material (PCM), reducing the complete melting time and enhancing the heat storage rate. Conversely, in the heat release process, an increase in steam mass flow rate and a reduction in inlet temperature expedite the solidification of PCM.

Key words: *phase change heat storage device; structural parameters; orthogonal test; optimization.*

1.Introduction

Renewable energy generation is characterized by its intermittency and randomness, which pose significant challenges to the stable operation of power grids. Consequently, an increasing number of coal-fired power plants are required to participate in power load regulation, taking on the task of peak shaving and filling, as well as accommodating the integration of renewable energy into the grid. The coupling of coal-fired power generating units and heat storage can not only provide more power consumption space for renewable energy power generation, but also is expected to decouple boilers and steam turbines, improve the operational flexibility of thermal power units, and thus make the load response more rapid.

Among various heat storage technologies, phase change heat storage (PCHS) is widely applied. Phase change materials (PCMs) offer several advantages, including a small temperature gradient, uniform heat storage, high heat storage density, and compact packaging of equipment. These benefits make PCMs one of the preferred choices for current heat storage technologies [1-4]. PCMs has unique competitive advantages in fields such as smart grids, molten salt energy storage for heating, the flexibility transformation of thermal power units and thermal-electric decoupling. Li *et al*. [5]

---

*Corresponding author; E-mail:54145299@qq.com conducted a simulation study on the peak-shaving capability of a 600 MW supercritical coal-fired unit's thermal system using a PCHS device under 3 heat storage strategies and 2 heat release strategies. Pang *et al.* [6] investigated the thermal performance and load response characteristics of a high-temperature molten salt heat storage device during heat storage and release processes for a double reheat unit boiler and turbine under rated conditions. Increasing the heat exchange area is an effective way to improve the performance of PCHS, for instance, by encapsulating PCMs in capsules or installing fins in the heat storage device. Due to their ease of manufacturing, many scholars have explored the impact of changing fin types and structural parameters to enhance heat storage performance. Cui *et al.* [7] analyzed the influence of the fin structure size on the heat storage/release performance of a phase-change heat exchanger. Hosseini *et al.* [8] explored the impact of different fin lengths and Stefan numbers on PCHS performance, demonstrating that increasing fin length results in more uniform temperature distribution and shorter melting times. Li *et al.* [9] conducted a numerical simulation of horizontally arranged longitudinal fins and found that thickening and lengthening the bottom fins improved the heat storage capacity of horizontal tubes, with the optimal model reducing the complete melting time by 54.1%. To improve the heat release performance of longitudinal fin latent heat storage devices during the late stages of solidification, Zhang *et al.* [10] used fractal tree-shaped fins, which maintained high efficiency throughout the solidification process, increasing the performance by 66.2%. They also optimized the fractal fins based on solidification time, and despite obstructing convection during the melting process, melting performance was still improved by 4.4%.

Although many studies have explored the impacts of structural parameters on the heat storage and release characteristics of annular fin heat storage devices, most of them have focused on controlling a single variable to assess these impacts. A comprehensive approach that considers multiple variables is essential as a first step toward analyzing the heat storage and release characteristics of such devices. Orthogonal tests [11-14] have been widely used in biology, engineering, and other fields to investigate the impact of multiple factors on experimental indicators. Regression orthogonal tests [15-16] build on orthogonal tests by establishing regression equations and conducting a series of validations and analyses, offering superior capabilities in studying quantitative relationships between multiple factors and experimental indicators.

Therefore, this paper focuses on the impact of basic geometric structural parameters of annular fins on the heat storage and release characteristics, using a three-variable quadratic regression orthogonal test to establish a regression equation. Through experimental analysis, the optimal structural parameters of the annular fin heat storage device were determined, and under these optimal conditions, the heat storage and release characteristics were studied for different operational parameters. The research results can provide inspiration for the technical route to improve the overall flexibility of coal-fired units after being coupled with phase change heat storage, and offer certain references for the flexible operation of thermal power plants.

2. Regression Orthogonal Test Study

2.1 Numerical calculation method

The subject of this study is an annular fin PCHS device, with its specific structural parameters in Fig. 1. High-temperature steam, serving as heat transfer fluid (HTF), is introduced into the heat storage device from the top of the central pipe, while the space outside the central pipe is filled with PCM, specifically a molten salt mixture of KCl(54)-46$ZnCl_2$. The height of PCHS device is 0.5 m, with an inner pipe radius denoted as $R_1(z_1)$, outer pipe radius R_2, fin thickness z_2, and fin length z_3. To ensure the engineering applicability and reliability of this orthogonal experiment, the structural parameters of the annular fin heat storage device (e.g., the inner pipe radius z_1, fin thickness z_2, and fin length z_3) were used to preliminarily determine the range of variations for each factor in the regression orthogonal test.

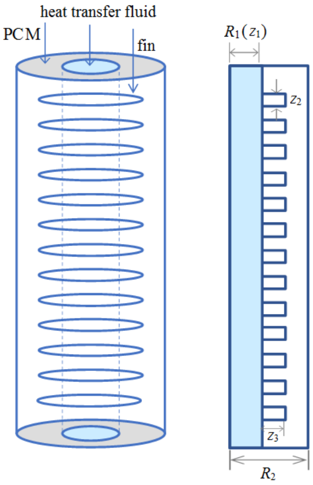

Fig. 1 Schematic diagram of annular fin heat storage device structure

In the simulation, the working fluid used is ideal water vapor, with the inlet of the computational domain defined by a mass flow rate boundary condition. The mass flow rate of the high-temperature steam at the inlet is set to 0.01 kg/s, with a temperature of 811 K. The initial temperature field of the entire heat storage device is set to 680 K. The coupling interface boundary conditions between the high-temperature steam, fins, and PCM are defined as continuous for both temperature and heat flux density, while the outer surface of the heat storage device is set to an adiabatic boundary condition. The standard k-ε model and SIMPLE algorithm are employed to solve the three-dimensional Navier-Stokes (N-S) equations for the flow field. ICEM software was used for modeling. When the grid spacing reached between 0.05 mm and 0.1 mm and the number of grid cells exceeded 950,000, the impact on the calculation of the liquid phase rate became negligible (Fig. 2). Therefore, to enhance computational efficiency, the number of grid cells used in each computational model in this study ranged between 950,000 and 1,000,000.

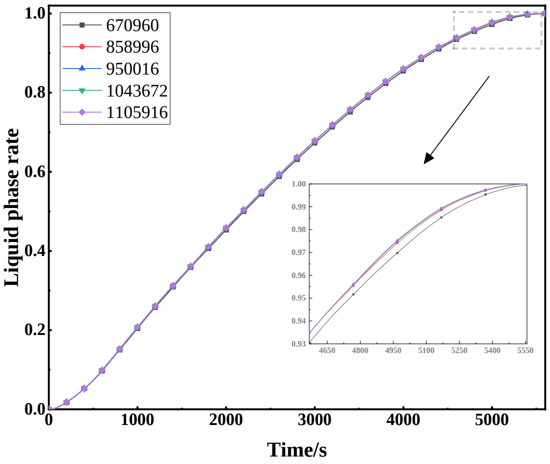

Fig. 2 Liquid phase rate varies with the number of grid cells

2.2 Regression orthogonal test design

In the regression orthogonal test, a limited number of test points were selected within the reasonable variation range of the factors to conduct simulation calculations and statistical analysis. Using this limited number of test points, a reliable regression equation was established. Once the structural parameters are determined, this regression equation can be used to estimate the corresponding heat storage capacity. By solving the regression equation within a specific range, the theoretical optimal values of the experimental factors that yield the maximum heat storage capacity can be obtained. This approach minimizes the need for extensive simulations and reduces the experimental workload, thereby improving the efficiency of the optimization design.

Table 1 Encode form of two levels and three factors

Level factors	Inner pipe radius z_1[mm]	Fin thickness z_2[mm]	Fin length z_3[mm]
Upper star arm (+*r*)	25	10.12	20
Upper level (+1)	23.41	9.06	18.41
Zero level (0)	18.91	6.06	13.91
Lower level (-1)	14.41	3.06	9.41
Lower star arm (-*r*)	12.82	2.00	7.82
Step size *⊿j*	4.5	3	4.5

To this end, this study adopts the three-factor quadratic regression orthogonal 1/2 fractional factorial method. According to the design principles of the heat storage device, the variation ranges of the three control parameters are determined as follows: z_1=12.82~25.00 mm； z_2=2.00~10.12 mm； z_3=7.82~20.00 mm. Let z_j (j=1, 2, 3) represent the factor levels in the regression orthogonal experiment, whereas z_{1j} and z_{2j} represent the upper and lower limits of each factor, with the zero level $z_{0j} = (z_{1j} + z_{2j})/2$. Based on the variation ranges of the factors, the level encoding is obtained (Tab. 1).

The number of test runs n required for the experiment is determined using Equation 1. Compared to a full factorial experiment, only 17 test runs are needed in this experiment, reducing the computational effort by 86.4%.

$$n = m_0 + m_c + m_r \tag{1}$$

where m_0 represents the number of center point trials (m_0=3); m_c represents the number of two-level factorial trials ($m_c = 2^p$); m_r represents the number of star point trials ($m_r = 2p$); and p represents the number of factors (p=3).

The length of the star arm is determined as follows:

$$r = (\sqrt{nm_c} - m_c)^{1/2} / \sqrt{2} \tag{2}$$

The variation intervals for the experimental levels can be determined based on the upper and lower limits of the factors and the length of the star arm.

$$\Delta_j = (z_{1j} — z_{2j})/2r \tag{3}$$

In an orthogonal test, all factors should maintain consistent units of measurement, and the variation between different factors should not be too large. To achieve this, the natural variables of each factor must undergo centralization processing. Let x_j represent the encoded value of each factor level after centralization, thereby $x_j = (z_j - z_{0j}) / \Delta_j$. The results of the experiment and their analysis are outlined in Tab. 2.

Table 2 Analysis of results of regression orthogonal experiments

Test	x_0	x_1	x_2	x_3	x_1x_2	x_1x_3	x_2x_3	$x_1'(x_1^2)$	$x_2'(x_2^2)$	$x_3'(x_3^2)$	Y[kJ]	y'[kJ]	Δ[%]
1	1	1	1	1	1	1	1	0.314	0.314	0.314	1636.803	1651.227	0.88
2	1	1	1	-1	1	-1	-1	0.314	0.314	0.314	1563.539	1563.862	0.02
3	1	1	-1	1	-1	1	-1	0.314	0.314	0.314	1622.977	1605.889	-1.05
4	1	1	-1	-1	-1	-1	1	0.314	0.314	0.314	1516.444	1518.524	0.14
5	1	-1	1	1	-1	-1	1	0.314	0.314	0.314	1604.788	1599.441	-0.33
6	1	-1	1	-1	-1	1	-1	0.314	0.314	0.314	1436.191	1453.652	1.22
7	1	-1	-1	1	1	-1	-1	0.314	0.314	0.314	1504.342	1486.844	-1.16
8	1	-1	-1	-1	1	1	1	1.145	-0.686	-0.686	1376.295	1341.055	-2.56
9	1	-r	0	0	0	0	0	1.145	-0.686	-0.686	1654.829	1641.001	-0.84
10	1	-r	0	0	0	0	0	-0.686	1.145	-0.686	1469.907	1485.911	1.09
11	1	0	r	0	0	0	0	-0.686	1.145	-0.686	1540.018	1541.732	0.11
12	1	0	-r	0	0	0	0	-0.686	-0.686	1.145	1452.036	1434.889	-1.18
13	1	0	0	r	0	0	0	-0.686	-0.686	1.145	1582.804	1586.609	0.24
14	1	0	0	-r	0	0	0	-0.686	-0.686	-0.686	1432.565	1428.88	-0.26
15	1	0	0	0	0	0	0	-0.686	-0.686	-0.686	1511.338	1507.744	-0.24
16	1	0	0	0	0	0	0	-0.686	-0.686	-0.686	1511.338	1507.744	-0.24
17	1	0	0	0	0	0	0	-0.686	-0.686	-0.686	1500.278	1507.744	0.45
D_j	17	11.66	11.66	11.66	8	8	8	6.70	6.70	6.70			
B_j	25916.5	668.35	340.30	679.72	-99.42	-116.85	7.28	204.06	-38.88	3.81			
b_j	1524.50	57.31	29.18	58.29	-12.43	-14.61	0.91	30.43	-5.80	0.57			
S_j		38305.31	9930.89	39619.6	1235.6	1706.7	6.63	6210.14	225.49	2.16			
F_j		939.39	243.54	971.62	30.30	41.85	0.16	152.30	5.53	0.05			
a_j		0.01	0.01	0.01	0.05	0.05		0.01	0.25				

By processing the data from the orthogonal table, the following unified form of the regression equation can be obtained as follows:

$$y = b_0 + \sum_{j=1}^{3} b_j x_j + \sum_{i<j} b_{ij} x_i x_j + \sum_{j=1}^{3} b_{jj} x_j x_j \tag{4}$$

where *y* represents the heat storage capacity, which is the response variable used as the performance metric in the experiment; *b* represents the constant term in the regression equation; b_j represents the linear regression coefficients for the main impacts (first-order regression coefficients); b_{ij} represents the partial regression coefficients for the interaction terms between different factors; and b_{jj} represents the quadratic regression coefficients (second-order regression coefficients).

The specific calculation formulas for the coefficients in the regression equation, based on the data in Tab. 2, are given as follows:

$$D_j = \sum_{j=1}^{n} (x_{ij})^2, \quad B_j = \sum_{j=1}^{n} x_{ij} y_j, \quad b_j = \frac{B_j}{D_j}, \quad S_j = B_j b_j, \quad F_j = \frac{S_j / f_j}{S_e / f_e} \tag{5}$$

where b_j represents the regression coefficient; S_j represents the sum of squares for each partial regression term; f_j represents the degrees of freedom for each partial regression sum of squares, all equal to 1; f_e represents the degrees of freedom associated with the experimental error.

The impact of the first-order terms on the heat storage capacity is ranked as x_3, x_1, x_2. The significance levels a_j for all three factors are 0.01, indicating that each factor significantly impacts the heat storage performance.

For interaction terms, the impact on heat storage capacity is ranked as x_1x_2 and x_1x_3, both with significance levels of 0.05. For second-order terms, the impact is ranked as x_1' and x_2', with significance levels of 0.01 and 0.25, respectively. The interaction x_2x_3 and second-order term x_3' had F-values smaller than $F_{0.1}$=(1,2), and were thereby excluded from the model.

Based on the calculations, the significance test result for the heat storage capacity regression equation is 44.89, which is greater than $F_{0.01}$=(7,9), indicating a high level of significance for the equation. Additionally, a lack-of-fit test, conducted using zero-level trials, yielded a value of 9.349, which is smaller than $F_{0.1}$=(7,2), confirming that the regression equation does not exhibit lack of fit. Therefore, the obtained regression equation is both highly reliable and demonstrates a strong fit to the experimental data.

2.3 Transformation and Validation of Regression Equation

Based on the previously described calculation methods and data processing, the corresponding encoded regression equation can be expressed as follows:

$$y = 1524.5 + 57.31x_1 + 29.18x_2 + 58.29x_3 - 12.43x_1x_2 - 14.61x_1x_3 + 30.43x_1^{'} - 5.8x_2^{'} \tag{6}$$

Based on experimental validation and optimization design, it is necessary to convert the encoded regression equation back into natural variables. This is done by applying the inverse centralization process to the encoded values using the centralization processing formula. The regression equation is then transformed into a function of the natural variables z_j, which correspond to the actual physical parameters in the experiment:

$$y = 1168.66 + 1.5z_1^2 - 1.18z_2^2 - 26.53z_1 + 51.01z_2 + 26.59z_3 - 1.25z_1z_2 - 0.72z_1z_3 \tag{7}$$

To verify the accuracy of the regression equation, the predicted heat storage values y' were calculated based on the regression equation for each experiment. The relative errors between the predicted and simulated values are shown in Tab. 2. The average relative error was found to be 0.69%, indicating that the regression equation is highly accurate and sufficiently reliable for engineering applications. By solving the regression equation, the optimal structural parameters were determined as follows: a high-temperature steam pipe radius of 12.823 mm, fin thickness of 10 mm, and fin length of 20 mm. Under these conditions, the heat storage capacity calculated through numerical simulation was 1647.548 kJ.

3. Optimization Design Results and Analysis

3.1 Analysis of optimization results for annular fin heat storage device

The heat storage capacity is the primary criterion for evaluating the performance of a thermal storage device. Fig. 3 compares the heat storage capacity, storage density, and liquid phase ratio at 5000s across different experimental trials. Since the total volume of the thermal storage device remains constant while the structural parameters vary, the mass of PCM differs between experiments. Therefore, it is necessary to select experiments with similar PCM mass for comparison. In Table 2, PCM mass in experiments 5, 12, and 14 is close to that in the optimal structural configuration. There, these three trials were selected for comparison with the optimal configuration. In Fig. 3, 1 represents the device with the optimal structure, while labels 2, 3, and 4 correspond to experiments 5, 12, and 14, respectively. The results show that both the heat storage capacity and heat storage density reached their maximum values under the optimal structural conditions. Compared to the other trials, the heat storage capacity increased by 2.60%, 11.87%, and 13.05%, respectively, while the heat storage density increased by 2.16%, 12.15%, and 12.57%. Furthermore, the liquid phase rate was also the highest under the optimal structural conditions, with increases of 2.07%, 12.66%, and 13.23% compared to the other trials. Phase change heat storage mainly completes energy storage by utilizing the melting process of PCM. The growth rates of heat storage capacity, heat storage density and molten salt liquid phase ratio obtained under the experiments are basically the same. Therefore, it can be considered that during the heat storage process, the increase in the molten salt liquid phase ratio is the main reason for the improvement of the heat storage performance of the phase change material.

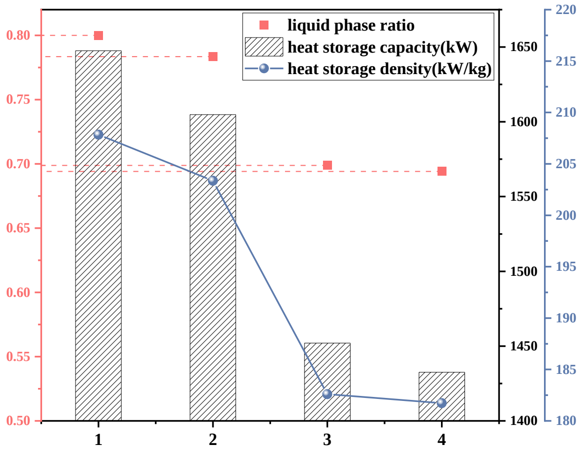

Fig. 3 Heat storage capacity, heat storage density and liquid phase ratio under different working conditions at 5000s

Under the optimal structural parameters, the phase change process within the annular heat storage device was studied, and its heat storage characteristics were analyzed. Fig. 4 illustrates the variation in the liquid phase rate of the heat storage salt. The liquid phase rate quantitatively indicates the melting degree of PCM, and the slope of the curve represents the rate of melting. In Fig. 4, the melting rate of PCM gradually decreases over time. This slowdown occurs because, as a portion of PCM melts, the liquid salt first absorbs heat from the high-temperature steam and transfers it to the remaining solid salt. The thermal diffusivity of liquid salt is lower than that of solid salt, causing the melting rate to slow as the volume of liquid salt increases, thereby reducing the amount of liquid salt produced per unit of time. Additionally, as the temperature difference between PCM and the high-temperature steam decreases, the heat storage performance diminishes, resulting in lower heat transfer efficiency, and the amount of heat absorbed by PCM continually decreases.

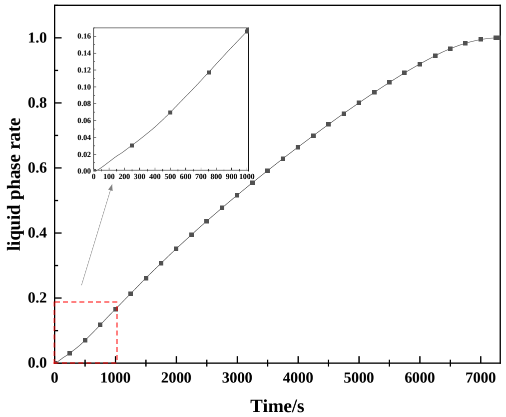

Fig. 4 Variation law of liquid phase rate of molten salt

Fig. 5 presents liquid phase distribution cloud maps at 2500 s, 3500 s, 4500 s, and 5500 s to analyze the melting characteristics of the annular fin PCHS device. The cloud maps illustrate that high-temperature steam enters from the top, transferring heat to PCM. The PCM begins to melt when its temperature rises to its melting point. The heat transfer process along the steam flow direction is continuous, with the upstream PCM consistently absorbing the heat from the high-temperature steam. As a result, the heat dissipates along the flow path, and the temperature decreases at different heights. The transition between solid and liquid phases is the primary characteristic of PCHS. In the thin layer at the solid-liquid interface, PCM exists in a mixed state, where both solid and liquid coexist. Although the solid-liquid interface occupies only a small portion of the total PCM volume, this mushy zone plays a crucial role in the phase change process by absorbing large amounts of latent heat to transform the solid into liquid. Due to the presence of the fins, the solid-liquid interface appears wavy. Over time, the interface gradually expands in the radial direction. At 5500 s, PCM has not fully melted, indicating that the melting rate is also impacted by the operational parameters of the heat storage device.

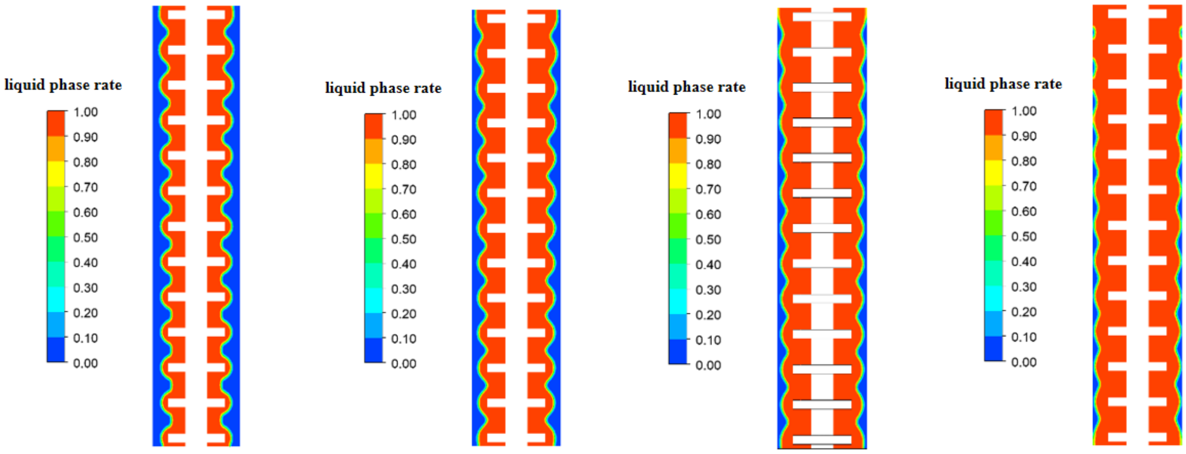

(a) 2500 s (b) 3500 s (c) 4500 s (d) 5500 s

Fig. 5 Liquid phase distribution at different times

3.2 Impact of operating parameters on heat storage characteristics of device

To analyze the impact of high-temperature steam mass flow rate on the heat storage process of the device, simulations were conducted under the condition that the high-temperature steam inlet temperature was set to 811 K, and the initial temperature field of the annular fin heat storage device was set to 680 K. The mass flow rates considered in the simulations were 0.01 kg/s, 0.015 kg/s, 0.02 kg/s, 0.025 kg/s, and 0.03 kg/s. Fig. 6 shows the variation in the liquid phase rate of PCM over time, as impacted by changes in the mass flow rate of the high-temperature steam. The slope of the curve represents the melting rate of PCM. At a mass flow rate of 0.03 kg/s, the melting rate is the fastest, while at 0.01 kg/s, the melting rate is the slowest. This indicates that the greater the mass flow rate of the high-temperature steam, the more heat is released by the heat source, and the faster PCM melts. At the same time point, the higher the mass flow rate, the higher the liquid phase rate of PCM. However, under the condition that the increase in mass flow rate is the same, the increase in the liquid phase ratio of the molten salt gradually decreases. This indicates that as the mass flow rate continues to increase, the extent to which the complete melting time of the molten salt decreases will become smaller and smaller, and the advantage of melting will also become less and less.

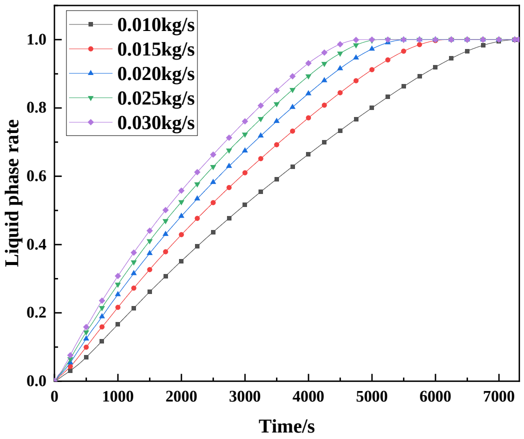

Fig. 6 Variation of liquid phase rate of molten salt under different mass flow rate

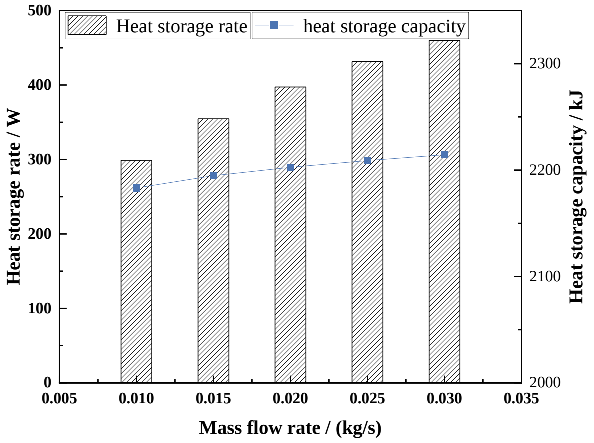

Fig. 7 Heat storage rate and heat storage under different mass flow rate

Fig. 7 depicts a comparison of the heat storage rate and heat storage capacity of the molten salt at the time of complete melting for different mass flow rates. The heat storage rates for mass flow rates of 0.01 kg/s, 0.015 kg/s, 0.02 kg/s, 0.025 kg/s, and 0.03 kg/s are 298.87 W, 354.71 W, 397.33 W, 431.44 W, and 459.93 W, respectively. As the mass flow rate increases, the rate of improvement in heat storage rate gradually diminishes. This is because the increase in mass flow rate will make the molten salt absorb more heat. Meanwhile, it will also shorten the residence time of high-temperature steam in the heat storage device. However, the molten salt absorbs energy in the form of latent heat at a relatively slow speed, and it takes a lot of time for the solid-liquid coexistence state to transition to the solid state. The mismatch of time scale will make the improvement range of the heat storage rate become smaller and smaller. The largest increase in heat storage rate, 18.68%, occurs when the mass flow rate is increased from 0.01 kg/s to 0.015 kg/s. This indicates that while increasing the mass flow rate optimizes the heat storage performance by enhancing the heat storage rate, the improvement becomes less significant as the flow rate increases further.

In Fig. 8, the variation in the liquid phase rate of PCM over time is impacted by different inlet temperatures of the high-temperature steam. When the inlet temperature increases from 801 K to 821 K, PCM melts more quickly, with the melting rate being the fastest at 821 K, where the liquid phase rate reaches 1 the earliest. At any given time, the melting ratio of PCM increases with higher inlet temperatures, and the difference in liquid phase rate between adjacent inlet temperatures is nearly the same. The increase in inlet temperature accelerates the melting process because the higher temperature steam, acting as the heat source, transfers more heat to PCM in the heat storage device. This allows

PCM to absorb more heat over the same period. Both increasing the mass flow rate and raising the inlet temperature enhance the melting process, but the impact of a 5 K increase in inlet temperature on the melting process is less significant than the impact of increasing the mass flow rate by 0.03 kg/s.

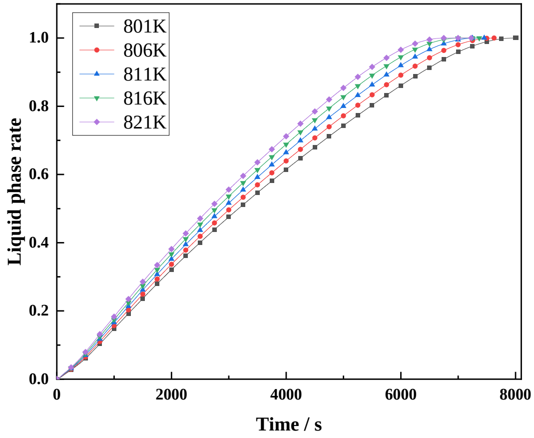

Fig. 8 Variation of liquid phase rate of molten salt at different inlet temperature

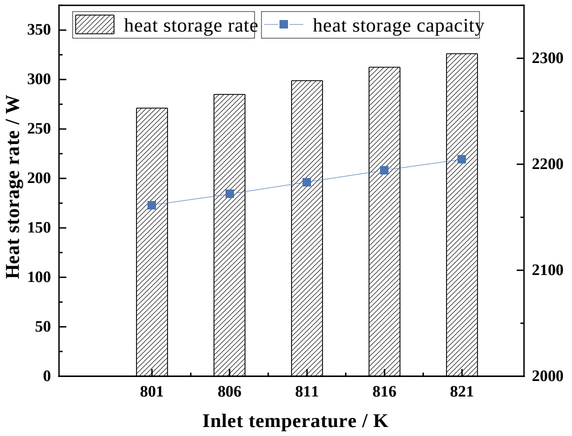

Fig. 9 Heat storage rate and heat storage capacity at different inlet temperature

Fig. 9 compares the heat storage rates and heat storage capacities at complete melting for different inlet temperatures. The heat storage rates at inlet temperatures of 801 K, 806 K, 811 K, 816 K, and 821 K are 271.12 W, 284.98 W, 298.87 W, 312.47 W, and 326.16 W, respectively. The largest increase in heat storage rate, 5.11%, occurs when the inlet temperature increases from 801 K to 806 K. For the subsequent intervals, the rate of increase gradually decreases: from 806 K to 811 K, the heat storage rate increases by 4.88%; from 811 K to 816 K, the increase is 4.55%; and from 816 K to 821 K, the increase is 4.38%. This indicates that raising the inlet temperature optimizes the heat storage performance, but the rate of improvement in heat storage rate gradually diminishes. The time required for complete melting has a significant impact on the heat storage rate, further demonstrating that the benefits of increasing inlet temperature taper off at higher values.

3.3 Impact of operating parameters on heat release characteristics of device

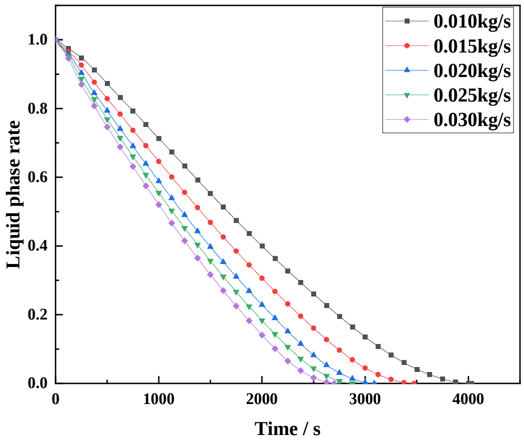

Fig. 10 Variation of liquid phase rate with different mass flow rates under exothermic condition

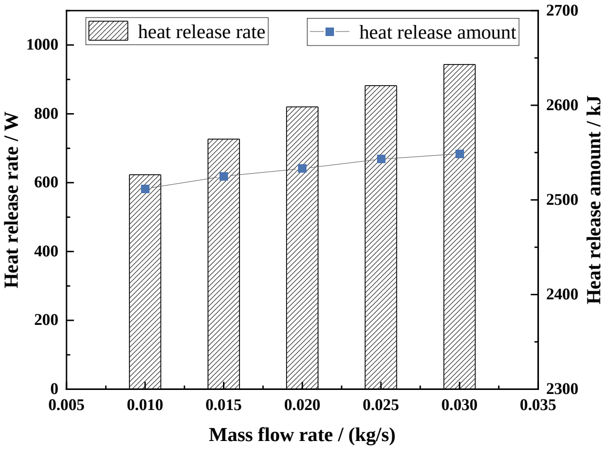

Fig. 11 Heat release rate and heat release of different mass flow rate

In Fig. 10, the variation in the liquid phase rate of PCM over time is impacted by changes in the mass flow rate of low-temperature steam, which can also be used to quantitatively analyze the degree of solidification. The slope of the curve reflects the rate of solidification, with the fastest solidification occurring at a mass flow rate of 0.03 kg/s and the slowest at 0.01 kg/s. This indicates that increasing the mass flow rate enhances heat transfer disturbances, allowing the low-temperature steam to absorb more heat from PCM. At any given time, as the mass flow rate of the low-temperature steam increases, the liquid phase rate of PCM gradually decreases, and the amount of solidified PCM increases. However, the increase in the amount of solidified PCM is not proportional to the increase in the mass flow rate. The variation in the liquid phase rate between different mass flow rates diminishes as the mass flow rate increases. It indicates that as the mass flow rate continues to increase, the extent to which the complete solidification time of the molten salt decreases will become smaller and smaller, and the advantage of solidification will also become less and less.

Fig. 11 presents a comparison of the heat release rate and heat release amount of the molten salt at complete solidification under different mass flow rates. Both the heat release rate and the heat release amount increase as the mass flow rate increases. However, the rate of increase in the heat release rate gradually diminishes, while the increase in the heat release amount remains relatively constant. This is because the latent heat released by the molten salt during complete solidification is fixed, whereas the sensible heat release is linearly related to the mass flow rate. The heat release rate is determined by both the total heat released and the time required for complete solidification. As the mass flow rate increases, the solidification time decreases, which in turn has a greater impact on the heat release rate. Therefore, the reduction in solidification time plays a more significant role in the variation of the heat release rate. The analysis shows that increasing the mass flow rate optimizes heat release performance, but the improvement in heat release rate diminishes as the flow rate continues to increase, indicating a point of diminishing returns for optimizing the heat release rate through mass flow adjustments.

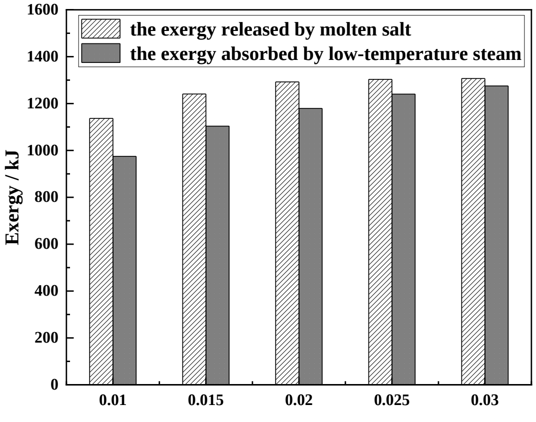

Fig. 12 Molten salt released exergy and steam absorbed exergy at different mass flow rates

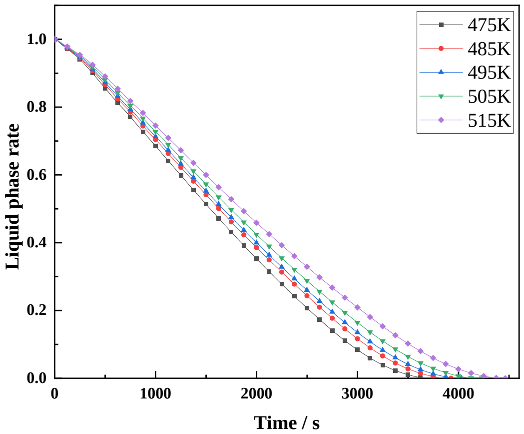

Fig. 13 Variation of liquid phase rate at different inlet temperature under exothermic condition

Fig. 12 illustrates the exergy released by the molten salt and the exergy absorbed by the low-temperature steam at different mass flow rates. The variation in the exergy released by the molten salt decreases as the mass flow rate increases, indicating that the impact of increasing mass flow rate on enhancing molten salt exergy release diminishes. After the molten salt has fully solidified, the curve flattens out because the sensible heat release from the molten salt per unit time is significantly reduced. In contrast, the exergy absorbed by the low-temperature steam increases with the mass flow rate, and the rate of increase remains fairly consistent. This shows that at a mass flow rate of 0.03 kg/s, the efficiency of energy absorption by the low-temperature steam is higher.

In Fig. 13, the variation in the liquid phase rate of PCM within the heat storage device over time is affected by different inlet temperatures of the low-temperature steam. The liquid phase rate of the molten salt increases with the increase in the inlet temperature, indicating that the solidification rate of the molten salt decreases with higher inlet temperatures. At an inlet temperature of 475 K, the solidification rate is the fastest, while at 515 K, the solidification rate is the slowest. This occurs because when the inlet temperature of the low-temperature steam is lower, the molten salt transfers more heat to the steam, which increases its own solidification rate.

Fig. 14 compares the heat release rate and heat release amount at the time of complete solidification of the molten salt under different inlet temperatures. When the inlet temperature is decreased, both the heat release amount and the heat release rate of the molten salt will increase. However, the variation range of the heat release rate first gradually decreases and then gradually increases after reaching the critical point of 495K. It can be seen that lowering the inlet temperature optimizes the heat release performance. As the inlet temperature decreases, the improvement in heat release performance initially slows down, but after reaching a critical point, the rate of improvement in heat release performance begins to increase.

Fig. 15 depicts the exergy released by the molten salt and the exergy absorbed by the low-temperature steam at different inlet temperatures. Over time, the exergy released by the molten salt accumulates, and as the inlet temperature decreases, the exergy release increases. As the inlet temperature drops from 515 K to 485 K, the difference between the adjacent curves gradually decreases. However, when the inlet temperature drops from 485 K to 475 K, the difference between the curves increases again. This indicates that as the temperature decreases, the incremental increase in exergy released by the molten salt diminishes, but after reaching a critical point, the incremental exergy release starts to increase again. Similarly, the exergy absorbed by the low-temperature steam also increases as the inlet temperature decreases. This means that by lowering the inlet temperature of the low-temperature steam, more heat can be extracted from the molten salt. Therefore, appropriately reducing the inlet temperature of the steam can enhance the energy transfer process, allowing for more efficient heat extraction from the molten salt, especially after the critical temperature threshold is crossed.

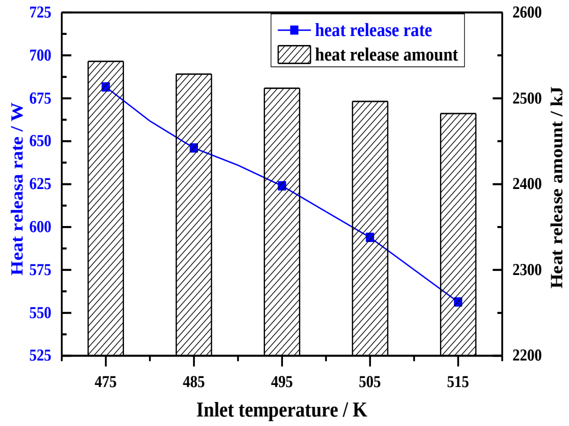

Fig. 14 Heat release rate and heat release at different inlet temperature

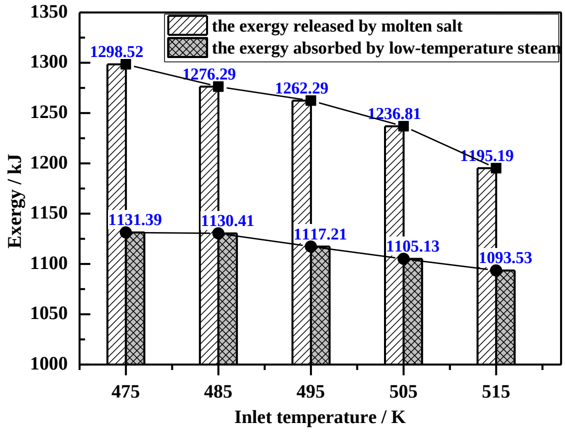

Fig. 15 Molten salt released exergy and steam absorbed exergy at different inlet temperaturen

4. Conclusions

(1) A regression equation for the structural parameters and heat storage capacity of the annular fin PCHS device was established using a three-factor quadratic regression orthogonal experiment. The equation passed both the significance and lack-of-fit tests. Within the range of factors considered in this study, the theoretical calculations from the formula were in good agreement with the experimental simulation results, meeting the requirements for practical engineering applications.

(2) The steam pipe radius, fin thickness, and fin length all have a significant impact on the heat storage capacity. The optimal structural parameters for maximizing heat storage capacity are a steam pipe radius of 12.823 mm, fin thickness of 10 mm, and fin length of 20 mm.

(3) During the heat storage process, increasing the mass flow rate and raising the steam inlet temperature both accelerate the melting of the molten salt, reducing the complete melting time and increasing both heat storage capacity and heat storage rate. However, the improvement in melting performance gradually diminishes as either the inlet temperature or mass flow rate increases. A 5 K change in inlet temperature has a smaller impact on melting performance compared to a 0.03 kg/s change in mass flow rate.

(4) During the heat release process, increasing the mass flow rate and lowering the inlet temperature accelerates the solidification of the molten salt, shortening the complete solidification time and increasing the heat release capacity, heat release rate, molten salt exergy release, and low-temperature steam exergy storage. As the inlet temperature decreases, the improvement in heat release performance initially slows, but after reaching a critical point, the improvement rate increases again.

5. References

[1] Haghighi, A., *et al*., Optimization of the thermal performance of PCM nanocomposites, *Journal of Energy Management and Technology*, 4(2020), 2, pp. 14-19

[2] Marri, G. K., *et al*., Experimental and numerical investigations on the effect of porosity and PPI gradients of metal foams on the thermal performance of a composite phase change material heat sink, *International Journal of Heat and Mass Transfer*, 164(2021), pp. 120454

[3] Weijian, Z., *et al*., Progress in the Study of enhanced heat exchange in phase change heat storage Devices, *ACS Omega*, 8(2023), 25, pp. 22331-22344

[4] Mohammad, B., *et al*., Experimental investigation of transient melting and heat transfer behavior of nanoparticle-enriched PCM in a rectangular enclosure, *Journal of Energy Storage*, 18(2018), pp. 485-497

[5] Li, D., *et al*., Study of supercritical power plant integration with high temperature thermal energy storage for flexible operation, *Journal of Energy Storage*, 20(2018), pp. 140-152

[6] Pang, L. P., *et al*., Flexibility improvement study on the double reheat power generation unit with a high temperature molten salt thermal energy storage, *Proceedings of the CSEE*, 41(2021), 8, pp. 2682-2690(in Chinese language)

[7] Cui, J., *et al*., Dynamic Numerical Study on Phase Change Thermal Storage Heat Transfer, *Thermal Science*, 25(2021), 6, pp. 4171-4179

[8] Hosseini, M. J., *et al*., Experimental and numerical evaluation of longitudinally finned latent heat thermal storage systems, *Energy & Buildings*, 99(2015), 10, PP. 263-272

[9] Li, H., *et al*., Influence of fin parameters on the melting behavior in a horizontal shell-and-tube latent heat storage unit with longitudinal fins, *Journal of Energy Storage*, 34(2021), 4, pp. 102230

[10] Zhang, C., *et al*., Improving the energy discharging performance of a latent heat storage (LHS) unit using fractal-tree-shaped fins, *Applied Energy*, 259(2020), 0, pp. 114102

[11] Energy and exergy performance analysis of a marine rotary desiccant air-conditioning system based on orthogonal experiment, *Energy*, 77(2014), pp. 953-962

[12] Su, L. S., *et al*., Identifying main factors of capacity fading in lithium ion cells using orthogonal design of experiments, *Applied Energy*, 163(2016), 1, pp. 201-210

[13] Wu, X., *et al*., Optimization of biodiesel production from camelina oil using orthogonal experiment, *Applied Energy*, 88(2011), 11, pp. 3615-3624

[14] Wei, L., *et al*., Hydraulic structure optimization of centrifugal pump based on orthogonal test, *Journal of Physics: Conference Series*, 2707(2024), pp. 012056

[15] Bo, Y., *et al*., Optimal Design of Orthogonal Test for Resistance Spot Welding, *Journal of Physics: Conference Series*, 2459(2023), pp. 012112

[16] Fang, X., *et al*., An adaptive functional regression-based prognostic model for applications with missing data, *Reliability Engineering & System Safety*, 133(2015), pp. 266-274

Paper submitted: 27.09.2024
Paper revised: 12.11.2024
Paper accepted: 19.11.2024